Computationally Efficient Retrieval of Snow Surface Properties From Spaceborne Imaging Spectroscopy Measurements Through Dimensionality Reduction Using k-Means Spectral Clustering

Brenton A. Wilder, Christine M. Lee, Adam Chlus, Hans-Peter Marshall, Jodi Brandt, Alicia M. Kinoshita, Josh Enterkine, Thomas Van Der Weide, and Nancy F. Glenn

***Abstract*—Snow albedo is a crucial component to the energy balance of our seasonal snowpack on Earth, reflecting incoming solar irradiance and altering the Earth system. Seasonal snow surface properties undergo constant change (e.g., melt-freeze cycle, faceting, sublimation, and windblown compaction) and have high spatial variability, especially in mountain regions, making it difficult to scale ground measurements. Snow albedo, fractional snow-covered area, and snow-specific surface area can be modeled using top of atmosphere radiance measurements from spaceborne imaging spectroscopy. We model these snow properties by testing inversions geared specifically for complex topography, as well as incorporating the impacts of the mixed snow pixel. Additionally, we avoid computing every pixel in an image by creating tens-of-thousands of k-means clusters based on the rounded values of the cosine of the local illumination angle to the nearest ten-thousandth digit. This computation is further sped up by leveraging message passing interface to scale with more nodes. We present this work as an open-source algorithm, which we refer to as Global Optical Snow properties via High-speed Algorithm With K-means clustering (GOSHAWK). We validate our algorithm with PRecursore IperSpettrale della Missione Applicativa *L*1 radiance imagery across eight sites in the Northern Hemisphere from 2021 to 2023 and compare outputs with field spectroscopy, specific surface area measurements, airborne LiDAR surveys, and four-component net radiometers. More work in algorithm development and calibration–validation work is needed in steep terrain and dense canopy to improve snow property retrieval prior to the Surface Biology and Geology and Copernicus Hyperspectral Imaging Mission for the Environment missions.**

Manuscript received 19 November 2023; revised 19 February 2024 and 22 March 2024; accepted 7 April 2024. Date of publication 9 April 2024; date of current version 25 April 2024. This work was supported by FINESST Award 21-EARTH21-0249. *(Corresponding author: Nancy F. Glenn.)*

Brenton A. Wilder, Hans-Peter Marshall, Josh Enterkine, Thomas Van Der Weide, and Nancy F. Glenn are with the Department of Geosciences, Boise State University, Boise, ID 83725 USA (e-mail: brentwilder@u.boisestate.edu; hpmarshall@boisestate.edu; joshenterkine@boisestate.edu; thomasvanderweide@boisestate.edu; nancyglenn@boisestate.edu).

Christine M. Lee and Adam Chlus are with the Jet Propulsion Laboratory, California Institute of Technology, Pasadena, CA 91125 USA (e-mail: christine.m.lee@jpl.nasa.gov; adam.m.chlus@jpl.nasa.gov).

Jodi Brandt is with the Human-Environment Systems, Boise State University, Boise, ID 83725 USA (e-mail: jodibrandt@boisestate.edu).

Alicia M. Kinoshita is with the Department of Civil, Environmental, and Construction Engineering, San Diego State University, San Diego, CA 92182 USA (e-mail: akinoshita@sdsu.edu).

This article has supplementary downloadable material available at https://doi.org/10.1109/JSTARS.2024.3386834, provided by the authors.

Digital Object Identifier 10.1109/JSTARS.2024.3386834

***Index Terms*—Imaging spectroscopy, optimization, snow albedo.**

I. Introduction

ANTHROPOGENIC climate change is warming high-latitude regions at a disproportionate rate compared with the rest of the globe [1], [2], [3]. For example, over the past century in Fairbanks, Alaska (United States), the onset of seasonal snowmelt has shifted earlier in the spring due to a temperature increase of 1.4 °C, which is nearly double compared with the rest of the globe during the same period [4]. Earlier spring snowmelt decreases the surface albedo earlier in the year, which in turn increases melt rates due to the well-known snow-albedo feedback [5]. An important step in improving resiliency and adaptation in the face of climate change is to reduce inaccuracies in the simulated snow-albedo feedback in Earth's global climate models [6]. Timely and accurate records of snow surface properties, such as albedo from satellite remote sensing, can help modeling and decision making across the globe [7], [8].

A widely used methodology for quantifying snow surface properties from remote sensing observations is the use of inversion algorithms, typically of a physically based set of equations with limiting assumptions [9], [10], [11]. Warren and Wiscombe [12] first presented a physically based set of equations that relates snow grain size, light-absorbing particles (e.g., soot and dust), and solar geometry to snow albedo. Warren and Wiscombe assumed that the scattering properties of each grain can be represented as a monodispersion of spheres using Mie single-scattering calculations [13]. However, recent studies have shown spherical assumptions to be problematic and can lead to inaccurate measurements of albedo [14]. A key assumption that many articles make is that the spectral albedo is equivalent to the observed sensor reflectance in the absence of a known bidirectional reflectance distribution function (BRDF) [9]. However, the asymptotic analytical radiative transfer (AART) theory [15] has provided a computationally efficient solution for weakly absorbing media to describe the single-scattering properties where grain shape can be nonspherical. Furthermore, this formulation accounts for BRDF, which is especially important for monitoring snow in complex terrain under variable lighting and viewing conditions. In this formulation, spectral snow reflectance r_{snow}

is a function of the cosine of the local solar illumination angle (μ_s), cosine of the local view angle (μ_v), phase angle (ξ), and wavelength (λ)

$$r0\left(\mu_s,\ \mu_v, \xi\right) = \frac{1.247+1.186(\mu_s+\mu_v)+5.157\mu_s\mu_v+\left(11^{(-0.087\xi)}+1.1^{(-0.014\xi)}\right)}{4(\mu_s+\mu_v)}$$

$$\alpha(\lambda)_{\text{snow}} = \exp\left(-\sqrt{\left\{\frac{4\pi k_{\text{ice}}(\lambda)}{\lambda} + \left(\frac{D}{b}\right)c\ \frac{4\pi k_{\text{soot}}(\lambda)}{\lambda}\right\}\left(\frac{6\times 16b}{\rho_{\text{ice}}\sigma\ \times\ 9(1-g)}\right)}\right)$$

$$r_{\text{snow}}\ \left(\mu_s,\ \mu_v, \xi, \lambda\right) =\ r0\left(\mu_s,\ \mu_v, \xi\right)\ \alpha^{f}_{\text{snow}}\left(\lambda\right) \tag{1}$$

where $r0$ represents the reflectance of the semi-infinite non-absorbing snow layer, α is the plane albedo, f is the escape function [15], k_{ice} is the imaginary refractive indices of ice, k_{soot} is the imaginary refractive indices of soot, D is the soot shape parameter of 1.3, b and g are the snow grain shape factors, c is the soot concentration, ρ_{ice} is the density of ice at 917 kg m^{-3}, and σ is the snow-specific surface area (SSA) in units m^2 kg^{-1}.

However, the pixels of global satellite products (~30 m) are highly mixed and can contain signals from surface features other than snow. To solve this, it is typical to solve a linear mixture model optimization problem containing pure endmembers that are common in the image, such as forest and rock. Alternatively, one could use a "snow-free" reference spectra of the pixel [9], although this could potentially include soil spectra where it is not present in the snow-covered pixel. For example, a snow-covered pixel could potentially have some forest, but the soil could still be covered by a few meters of snow, thus limiting the effectiveness of such a mixing strategy. One may solve for the snow properties and fractional covers simultaneously by using constrained numerical optimization methods to minimize the difference between the modeled and observed signal for a pixel, given that spectral albedo is equivalent to surface reflectance. Bair et al. [9] increase the speed of this method by a factor of 50 by grouping similar pixels based on snow-free spectra, snow spectra, and μ_s above a threshold tolerance of 0.05 (unitless).

Another approach shown by Bohn et al. [16] solves for snow properties and atmospheric properties simultaneously. Bohn et al. [16] develop a gridded MODTRAN lookup table and solve for top of atmosphere (TOA) radiance by allowing spectral reflectance (which is also assumed to be spectral albedo) and atmospheric parameters aerosol optical depth and precipitable water to vary in optimization. The authors test this framework in Greenland where slopes are mild, and therefore, influences from terrain are neglected.

We expand the work of others by developing an open-source algorithm for the snow science community, Global Optical Snow properties via High-speed Algorithm With K-means clustering (GOSHAWK). This algorithm is computationally efficient and takes advantage of the full spectrum of data provided by imaging spectroscopy, such as the datasets to be collected by Surface Biology and Geology (SBG) and Copernicus Hyperspectral Imaging Mission for the Environment (CHIME). Similar to Bair et al.'s article [9], we employ a clustering technique; however, we leverage k-means unsupervised spectral clustering across each image dependent on μ_s. Another improvement we make is the incorporation of AART, which allows for more diverse grain shapes and accounts for BRDF. We also make improvements by solving for atmospheric and surface states simultaneously in a similar way to Bohn et al.'s article [16] but include information about the topography and mixed pixel. Finally, we develop GOSHAWK to use message passing interface (MPI) to quickly distribute optimization tasks across several nodes on a Linux cluster. In the following sections, we describe the algorithm and assess its accuracy at eight sites in the Northern Hemisphere.

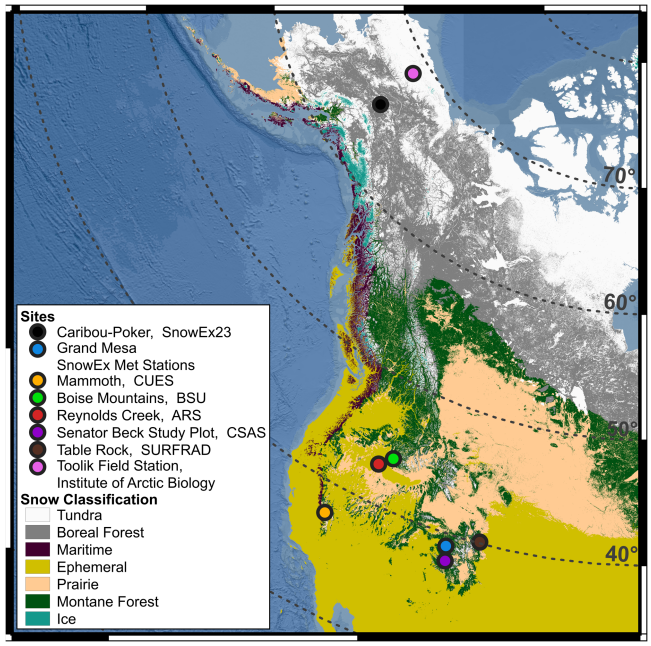

Fig. 1. Location of validation sites, including caribou-poker creeks research watershed via NASA SnowEx 2023 campaign, SBSP via Center for Snow and Avalanche Studies (CSAS), Grand Mesa Meteorologic Stations via NASA SnowEx, Mammoth mountain via the Cold Regions Research and Engineering Laboratory and University of California Santa Barbara energy site (CUES), Boise Mountains via Boise State University, table rock via surface radiation network (SURFRAD), Reynolds Creek via agricultural resource services (ARS), and Toolik Field Station via Institute of Arctic Biology. Validation sites are plotted with respect to a snow classification map [17].

II. Methods—GOSHAWK Algorithm

GOSHAWK is an open-source algorithm developed in Python (v3.10) and optimized for execution on large Linux clusters. In this study, we ran the algorithm on a Linux cluster in which each node was equipped with 192 GB of memory and 48 Intel Xeon Gold 6252 2.10 GHz processors. We tested GOSHAWK on 17 images across eight different sites throughout North America (see Fig. 1). Across the eight sites, five were classified as montane forest (Mammoth, Boise Mountains, Reynolds Creek, Senator Beck Study Plot (SBSP), and Grand Mesa), with the surface being mostly characterized by new and recent snow throughout the winter [17]. The other three included an ephemeral site (Table Rock) where the typical surface includes ice lenses and percolation columns, a boreal forest site (Caribou-Poker) where the typical surface includes new and recent snow, and a tundra

TABLE I
ALL TERRAIN AND GEOMETRY PARAMETERS COMPUTED FOR EACH PIXEL

Symbol	Definition
μ_s	Cosine of the local solar illumination angle
μ_v	Cosine of the local view angle
ξ	Phase angle
θ_0	Solar zenith angle
θ_v	View zenith angle
ϕ	Relative azimuth angle
V_Ω	Sky view factor
ψ	Shade binary mask
S	Terrain slope

site (Toolik Field Station) where the typical surface includes wind slabs. In the following sections, we discuss the major components of our algorithm, including the preprocessing, numerical optimization, and postprocessing step. A workflow diagram of the algorithm is provided in the supplementary documents (see Fig. S.1).

A. Dataset Integration

GOSHAWK is programmed to download relevant ancillary data, which are reprojected based on the bounds and projection of the input image. The first is the digital elevation model (DEM), which has the option to originate from Copernicus, United States Geological Survey 3DEP, or NASA Shuttle Radar Topography Mission. Land cover data are downloaded from the European Space Agency (ESA) WorldCover 10 m 2020 land cover class [18]. Canopy cover fraction data are downloaded from Moderate Resolution Imaging Spectroradiometer vegetation continuous fields product collection 6, Version 1 [19]. The canopy cover fraction data are assumed to be consistent with most spaceborne imaging spectroscopy acquisitions near-nadir viewing angles.

B. Topographic Calculations

After ancillary data are acquired, relevant topographic and geometric parameters are computed (see Table I). The sky view fraction (V_Ω) is computed via Dozier and Frew [20]. The shade binary mask (ψ) is computed using the ray-tracing algorithm presented in this study and occurs whenever the topography interrupts the vector between the observer pixel and sun position (see Fig. S.2). Local illumination and local view angles are computed using all the relevant terrain and observation data (see Table I).

C. Cloud Masking

Determining pixels as cloud or snow is still an active area of research in the snow science community [21]. Therefore, we present a simple thresholding approach for images in our study (see Fig. S.3). If radiance at 1994 nm$>$ 0.13 μW cm^{-2} nm^{-1}sr^{-1}, radiance at 2490 nm$>$ 0.12 μW cm^{-2} nm^{-1}sr^{-1}, and max radiance at any wavelength is $>$ 13 μW cm^{-2} nm^{-1}sr^{-1}, the pixel is marked as a cloud. The thresholds at 1994 and 2490 nm were selected based on the absorption properties of snow at these wavelengths. A similar threshold approach using raw radiance data has been performed [22]. We justify this simpler, computationally inexpensive approach because clouds minimally impacted the findings of this study. The imagery was downloaded with generally low cloud cover (see Fig. S.3). However, while we ignore clouds in our study, we acknowledge they significantly impact snow remote sensing. Our simple thresholding method may fail in applications outside of this analysis. Our main focus is evaluating cloud-free pixels, and future work could incorporate more sophisticated cloud masks quite easily into our framework.

TABLE II
LIBRADTRAN COMBINATIONS USED TO BUILD LOOKUP TABLE

/ # Parameter	1	2	3
H_2O [mm]	1	25	50
AOD550 [unitless]	0.01	0.5	1.0
Altitude [km]	min	max	-
θ_0 [°]	mean	-	-
θ_v [°]	mean	-	-
ϕ [°]	mean	-	-

Min, max, and mean represent values for the given image.

D. Atmospheric Parameters

We ran libRadtran version 2.0.4 [23] for each image for 18 different simulations of precipitable water (H_2O), aerosol optical depth at 550 nm (AOD550), and altitude using DISORT (streams $= 16$) while keeping θ_0, θ_v, and ϕ constant to reduce computational load (see Table II). The resulting sparse lookup table is gridded using SciPy RegularGridInterpolator with respect to H_2O, AOD550, altitude, and image sensor wavelengths (λ). The RegularGridInterpolator object is saved in the pipeline for use during numerical optimization to quickly interpolate the derived atmospheric parameters for use in (3).

E. k-Means Spectral Clustering and Parallel Computing

To scale the algorithm for global applications, we implement unsupervised learning in the form of k-means spectral clustering with the Spectral Python package.[1] The k-means spectral clustering is performed by solving for a maximum of ten clusters (max iterations $= 100$) for every ten-thousandth place of μ_s. While μ_s is allowed to range from -1 to 1 to increase classes at this stage, we corrected it to range from 0 to 1 in numerical optimization (i.e., constrained to real bounds of μ_s). This results in tens of thousands of unique spectral classes, with the exact number depending on the terrain and surface features in the image. However, we present this as a set of three tunable parameters in the function (number of clusters, max iterations, and μ_s decimals). These spectral classes are mapped back to their

[1][Online]. Available: https://github.com/spectralpython/spectral

real-world pixel location to obtain topographic information. All relevant topographic and land surface parameters are aggregated by averaging with respect to each k-means class, including altitude, μ_s, μ_v, ξ, S, and V_Ω, land cover code, and ψ. Landcover code and ψ are rounded to the nearest tens place and nearest ones place, respectively. This produces a flattened array of classes for optimization.

We simultaneously pass this aggregated array to our numerical optimization routine using MPI via MPI4py [24], [25]. The major advantage of our algorithm is that the code is built around MPI, where each element of the array is independent and, therefore, allows the algorithm to scale with more computational resources. For example, using four compute nodes (total of 192 CPUs), the numerical optimization routine takes under 15 min for an image of approximately 1 million pixels (exact time depends on the image).

F. Numerical Optimization

In retrieval of snow properties, it is a common practice to use a linear mixture model containing four or fewer distinct endmembers [9], [26]. We used snow, shade, and two other spectra based on the pixel values of the land cover map. The shade endmember was selected due to the common unknown localized surface topography that can occur in snowy terrain [27]. The surface spectra for the two dependent endmembers (r_{LC_1} and r_{LC_2}) are selected programmatically from EcoSpecLib Version 1 [28] based on the land cover at the pixel. This allows us to derive a surface reflectance (r_{surf}), defined as follows:

$$r_{\text{surf}}(\lambda) = r_{\text{snow}}(\lambda) f_{\text{snow}} + r_{\text{shade}}(\lambda) f_{\text{shade}} + r_{LC1}(\lambda) f_{LC1} + r_{LC2}(\lambda) f_{LC2} \quad (2)$$

where r_{surf} is the observed directional reflectance from the satellite, r_{snow} is computed iteratively from (1) during optimization, r_{shade} is the photometric shade and is a constant zero with respect to λ, and f_{snow}, f_{shade}, f_{LC1}, and f_{LC2} are the fractional covers of each endmember. A linear mixture is an imperfect assumption, especially for areas of dense canopy where multiple scattering between surfaces can occur before the light returns to the sensor [29]. However, nonlinear mixing is challenging because of missing information and mathematical complexities [30], and therefore, like Bair et al.'s work [9], we use a linear assumption. We also note that r_{LC_1} and r_{LC_2} are pure endmember reflectance derived in labs that do not account for directional reflectance, which can be considered for future algorithm improvement. On the other hand, r_{snow}, which is derived from (1), *does* account for directional reflectance. We fix the snow grain shape to be $g = 0.75$ and $b = 1.6$. It is worth noting that these may be tuned based on the prior knowledge of the expected snow grain shape. For the refractive index of ice, we use a composite method that is modulated by the refractive index of water by solving the fraction of liquid water content (LWC) present [31], [32], [33], [34].

The derived surface reflectance r_{surf} is used in (3) iteratively to minimize root mean squared error (RMSE). We employ a quasi-Newton method (Broyden–Fletcher–Goldfarb–Shanno algorithm) applied to a Lagrange function (SciPy's sequential least squares programming method [35]) to minimize RMSE(ε) across all valid bands (i.e., excluding common atmospheric absorption bands)

$$\begin{aligned} E(\lambda) &= \psi\mu_s E(\lambda)_{\text{dir}} + V_\Omega E(\lambda)_{\text{diff}} \\ &\quad + \left[\left(1 + \frac{\cos(S)}{2} - V_\Omega\right) r(\lambda)_{\text{surf}} \left(E(\lambda)_{\text{dir}} + E(\lambda)_{\text{diff}}\right)\right] \\ L(\lambda)_{\text{TOA, Pred}} &= L_0 + \frac{1}{\pi} \frac{r(\lambda)_{\text{surf}} E(\lambda) T(\lambda)^{\uparrow}}{1 - \Theta(\lambda) r(\lambda)_{\text{surf}}} \\ &\text{minimize RMSE}[L(\lambda)_{\text{TOA, Pred}},\ L(\lambda)_{\text{TOA, Obs}}] \end{aligned} \quad (3)$$

where E_{dir} is the direct irradiance, E_{diff} is the diffuse irradiance, $T^{\uparrow}$ is the total upward atmospheric transmittance, Θ is the spherical albedo at the bottom of the atmosphere, and L_0 is the atmospheric path radiance, all of which are interpolated from the lookup table created by the libRadtran in the preprocessing step. In this formulation, the nearby pixels that contribute to the terrain-reflected radiation are equal in surface reflectance to the target pixel. This assumption must be made due to the dimensionality reduction and is a fair assumption where there is likely snow cover surrounding the target pixel if the target pixel is snow covered.

We supply constraints to the optimization by ensuring fractional covers sum to 1, single cover ranges from 0 to 1, and all other parameters vary within realistic boundaries (see Table III). In the final step after optimization, we also compute snow broadband albedo, which is defined as the ratio of surface upward radiation flux to the downward radiation flux within 400–2500 nm [36]. The downward radiation flux in this case is optimal $E(\lambda)$ computed in (3).

G. Postprocessing

There are physical limitations to the use of optical sensors, especially in steep, forested terrain, to retrieve snow surface properties, even with the added information from imaging spectroscopy. Therefore, we use a threshold of over 50% canopy cover to assign no data values for all parameters [37]. Also, when the modeled reflectance normalized difference in snow index is less than 0.0, the pixel is returned as no snow. Then, we determined if the initial f_{snow} is less than 75%, we return only the fractional covers (no snow properties), similar to Bair et al.'s article [9]. This results in many null data depending on the image. During postprocessing, images are interpolated to coarser resolution depending on user input. The fractional snow cover estimated is adjusted to account for the terrain and canopy. We used (4) to estimate fractional snow-covered area (fSCA) [9]

$$\text{fSCA} = \min\left[1, \frac{f_{\text{snow}}}{1 - f_{\text{shade}} - f_{\text{canopy cover}}}\right]. \quad (4)$$

TABLE III
LIGHT-ABSORBING PARTICLES [ng g^{-1}]

Parameter [unit]	Definition	Feasible Range	Initial State
f_{snow} [%]	Fractional snow in the mixed pixel	[0, 100]	10
f_{shade} [%]	Fractional shade in the mixed pixel	[0, 100]	20
f_{LC1} [%]	Fractional cover of endmember 1 (based on land cover value at pixel)	[0, 100]	50
f_{LC2} [%]	Fractional cover of endmember 2 (based on land cover value at pixel)	[0, 100]	20
Specific Surface Area [m^2 kg^{-1}]	Related to the optical grain size at the snow surface via the density of ice	[2, 156]	40
Light-Absorbing Particles [soot]	Concentration of light-absorbing particles modeled as soot.	[0 - 5000]	0
LWC [%]	Percentage of LWC in the snowpack.	[0, 20]	2
AOD550 [%]	dimensionless Aerosol Optical Depth at 550 nm	[1,100]	10
H_2O [mm]	Precipitable water vapor in the atmosphere	[1,50]	1

III. VALIDATION METHODS

A. Remote Sensing Imagery

In this study, we selected *PRecursore IperSpettrale della Missione Applicativa* (PRISMA) as input into our algorithm for testing because it represents similar data to SBG and CHIME. PRISMA is a satellite launched by the Italian Space Agency (ASI) that began operation on 22 March 2019. PRISMA measures radiance in 239 bands between 400 and 2500 nm at a spectral resolution better than 12 nm across the visible and near infrared (VNIR) and shortwave infrared (SWIR). PRISMA radiance across VNIR and SWIR compared with in situ measurements across agricultural sites in Italy has an error less than 5% [38]. PRISMA spatial resolution is approximately 30 m. The revisit time is 29 days from nadir, with the capability for shorter, off-nadir revisit times (7 days) via a roll maneuver. PRISMA L1 datasets exhibited spatial misregistration errors upon first inspection (see Fig. S.4). To ensure that remote and in situ datasets and topography datasets were colocated, PRISMA images were geometrically corrected using an image matching algorithm [39]. Using a Sentinel-2 NIR weekly mosaic as a reference image, PRISMA pixel coordinates were adjusted to maximize the correlation between the reference image and target PRISMA NIR image. After alignment, there are artifacts present along ridges and change in slope direction. This is caused by slight spatial misalignment in the DEM with respect to the imagery [40] and will be addressed in our future work. In this study, we use 17 PRISMA L1 TOA radiance images spanning 2021–2023 where there were coincident field measurements (see Table IV).

Imagery data were focused on a wide variety of snow conditions, including steep forested terrain in Boise Mountains (Idaho,

TABLE IV
PRISMA IMAGES USED IN STUDY

PRISMA scene name	Site, Source
PRS_L1_STD_OFFL_20210123184757_20210123184801_0001	Reynolds Creek, ARS
PRS_L1_STD_OFFL_20210321213723_20210321213727_0001	Toolik Field Station, Institute of Arctic Biology
PRS_L1_STD_OFFL_20210331180442_20210331180446_0001	SBSP, CSAS
PRS_L1_STD_OFFL_20210406180740_20210406180744_0001	Grand Mesa SnowEx Met Stations
PRS_L1_STD_OFFL_20210429180418_20210429180422_0001	SBSP, CSAS
PRS_20220129184504_20220129184509_0001	Boise Mountains, Boise State
PRS_L1_STD_OFFL_20220210185335_20220210185339_0001	Boise Mountains, Boise State
PRS_20220215184018_20220215184022_0001	Boise Mountains, Boise State
PRS_L1_STD_OFFL_20221121185001_20221121185006_0001	Boise Mountains, Boise State
PRS_L1_STD_OFFL_20221115184830_20221115184835_0001	Mammoth, CUES
PRS_L1_STD_OFFL_20221208184337_20221208184341_0001	Boise Mountains, Boise State
PRS_L1_STD_OFFL_20221214184840_20221214184845_0001	Mammoth, CUES
PRS_L1_STD_OFFL_20230124185459_20230124185503_0001	Mammoth, CUES
PRS_L1_STD_OFFL_20230210184839_20230210184843_0001	Mammoth, CUES
PRS_L1_STD_OFFL_20230224175101_20230224175106_0001	Table Rock, SURFRAD
PRS_L1_STD_OFFL_20230317185151_20230317185155_0001	Mammoth, CUES
PRS_L1_STD_OFFL_20230315212501_20230315212506_0001	Caribou-Poker, SnowEx23 Campaign

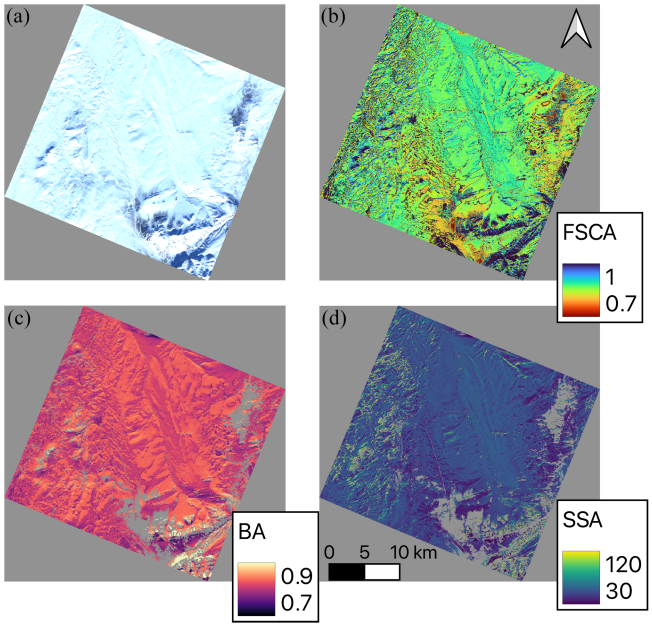

Fig. 2. (a) PRISMA L1 TOA radiance true colors. (b) fSCA. (c) Snow broadband albedo. (d) SSA for an image near Toolik Field Station on 21 March 2021. Gray represents no data regions. All rasters shown here are at native 30 m spatial resolution. We chose this one to highlight the challenging solar illumination and view conditions ($\theta_{0,\,\mathrm{AVG}} = 68.1°$; $\theta_{v,\,\mathrm{AVG}} = 10.4°$) and shallow snow conditions.

USA), deep snowpacks in the Sierra Nevada Mountains (California, USA), and shallow snowpacks in arctic tundra (Alaska, USA). Fig. 2 illustrates the calculated values from (1–4) for 21 March 2021 Toolik Field Station image.

B. In Situ Field Validation

Continuous four-component radiometer measurements were also collected for several sites across North America [41], [42], [43], [44], [45], [46] (see Fig. 1). These datasets were used to evaluate the estimated snow broadband albedo across a wide range of sites. Coincident retrieved PRISMA properties were sampled at 3×3 nearest neighbor to convey possible uncertainties in the retrieval. Net radiometer measurements were only used in cases where the ground cover footprint was completely snow covered (see Fig. 3). This was done to avoid potentially bad validation data that captures both soil and snow. We used a combination of on the ground imagery, snow depth sensor measurements, and other historical data to ensure high confidence that net radiometer footprints were entirely snow covered. An uncertainty of +/−2% was assumed for the observed albedo based on calibration uncertainty less than 3% for a given net radiometer [47]. Without prior knowledge of the radiometer for each site, we determined that a generalized uncertainty was most appropriate.

In situ field measurements in the Boise Mountains, ID (USA) were collected using an ASD FieldSpec4 (Malvern Panalytical, calibrated in summer 2022) [46]. ASD FieldSpec4 spectral reflectance measurements were collected with the bare fiber fore optic held level 1 m off flat surface. White Spectralon panel reference measurements were taken prior to each measurement. ASD FieldSpec4 albedo measurements were collected with the remote cosine receptor fore optic held level at 1 m off the surface following the protocol of Carmagnola et al. [48] and were corrected for small terrain effects [48], [49] (see Fig. S.5). All ASD FieldSpec4 measurements were collected within 24 h of the start time of the PRISMA acquisition and near solar noon (+/−1 h). An overall uncertainty of 1% was used for the albedo measurement [50].

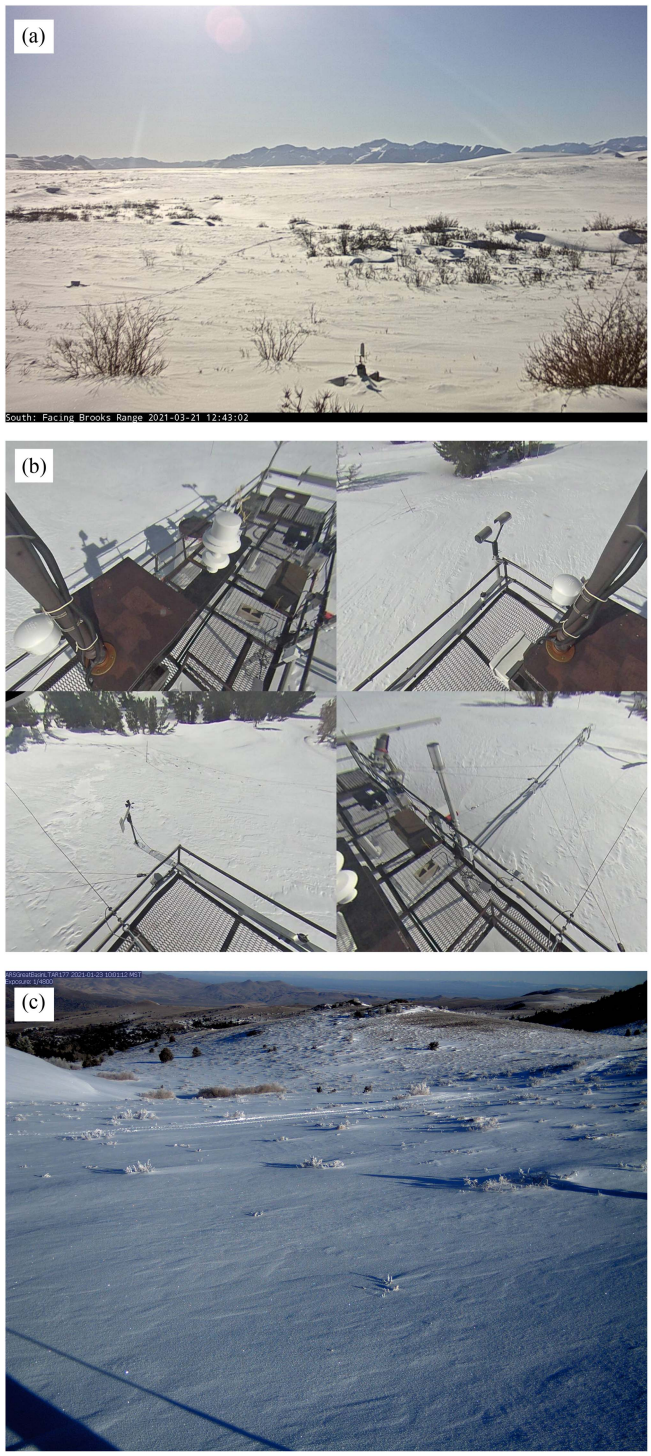

Fig. 3. Ground imagery at (a) Toolik field station on 21 March 2021, (b) CUES on 10 February 2023, and (c) Reynolds Creek site on 23 January 2021, shared courtesy of Andrew Hedricks, ARS.

To compare retrieved SSA, we used coincident PRISMA imagery (+/−24 h) at Caribou Poker Creeks Research Watershed with NASA SnowEx23 IceCube field measurements [51]. IceCube measurements were taken at varying depths, separated by roughly 10 cm. Two nearby pits were sampled (EA229_ICECUBE_v01 and EB227_ICECUBE_v01). In our assessment of PRISMA retrieved SSA, we compared modeled nearest neighbor values and standard deviations to the average surface measurements of both IceCube observations (depth = 0 cm). We note that these IceCube observations were taken under dense boreal forest, and therefore, it is assumed that our accuracy will be less than that of an open area. We interpolate the retrieved PRISMA SSA to 1000 m spatial resolution in this comparison.

Coincident helicopter airborne LiDAR was collected at the Boise Mountains site for the PRISMA acquisition on 8 December 2022 [52]. No ground control points were used during the flights, so to ensure correct alignment, we used QGIS to digitize a polygon of the road surface that runs through the site based on the best available airborne LiDAR data. This road polygon was used to run an iterative closest point via the Ames Stereo Pipeline [53] to find an optimal translational and rotational matrix for tie points over the road surface between snow-free and snow-on LiDAR data. This rotational and transformation matrix for the clipped road LiDAR was then applied to the entire airborne LiDAR dataset for a given acquisition. The general underlying assumption is that snow is plowed regularly on the state highway intersecting the flights, and thus, the points within the road polygon are the same between snow-free and snow-on conditions (see Fig. 4). This methodology is presented as an open-source tool, *ice-road-copters* in GitHub [54]. We used a helicopter LiDAR flight from 8 December 2022 because it was coincident with PRISMA.

The LiDAR acquisition was classified as snow if the depth was greater than 8 cm [37]. To validate fSCA, we use the RMSE and average bias between the classified LiDAR and the retrieved fSCA interpolated to 100 m. Since we are only interested in the presence or absence of snow and using a much coarser resolution than the original LiDAR dataset, we assume minimal impact from LiDAR coregistration error on our analysis. We chose to interpolate in this comparison because dense forest cover can produce no data regions, and thus, we elect to resample to improve the estimate under the canopy. Additionally, we compute snow detection performance, a binary estimate that is based on whether the fSCA is greater than 0% for a given pixel, indicating snow is present. To validate this result, we create binary datasets by using this 0% threshold for snow or no snow. Then, we compute the F-stat using the following equation [36]:

$$\text{Fstat} = \frac{2\left(\frac{\text{TP}}{\text{TP+FP}}\right)\left(\frac{\text{TP}}{\text{TP+FN}}\right)}{\left(\frac{\text{TP}}{\text{TP+FP}}\right)+\left(\frac{\text{TP}}{\text{TP+FN}}\right)} \tag{5}$$

where true positive (TP) is when a pixel is correctly predicted as snow, false positive (FP) is when a pixel is incorrectly labeled as snow when there is no snow present, and false negative (FN) is when a pixel is incorrectly labeled as no-snow when there is snow present.

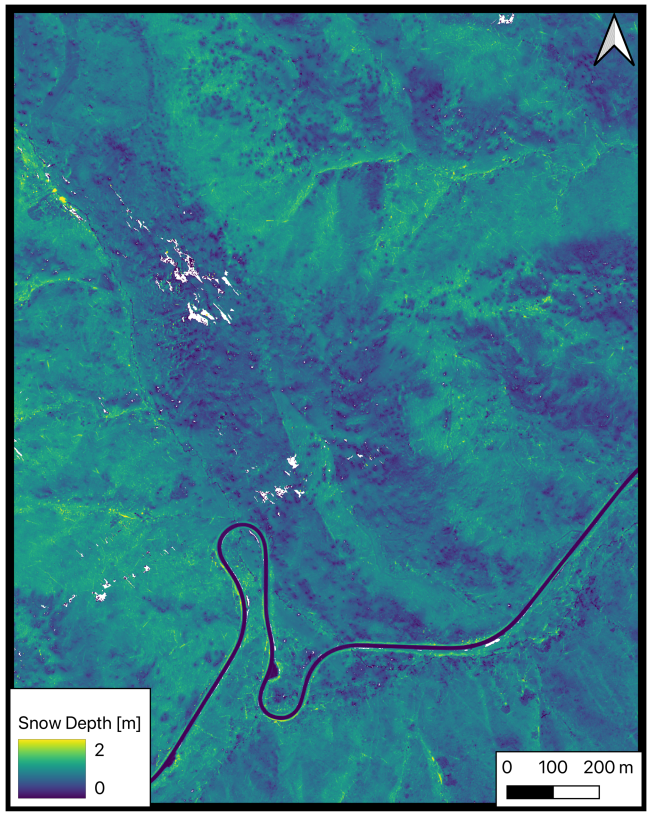

Fig. 4. Subset of processed 0.5 m resolution LiDAR product from ice-road-copters for 8 December 2022, specifically highlighting the road free of snow. This acquisition was taken at Mores Creek Summit in the Boise Mountains, Idaho (USA).

IV. Validation Results

Modeled broadband albedo results were compared with the tower-based four-component radiometer measurements at seven sites between 2021 and 2023 (see Fig. 5). We found good agreement between the modeled broadband albedo and the observed broadband albedo (R^2 = 0.86; RMSE = 0.024; mean bias = 0.009; and samples = 14). Many of the sites exhibit high spatial variability at the 30 m scale (see Fig. 5; vertical error bars).

Spectral reflectance with the ASD bare fiber fore optic was collected at Idaho City Football Field (Boise Mountains) coincident with PRISMA imagery on 10 February 2022 [see Fig. 6(a)]. The total RMSE for the modeled snow endmember reflectance across the entire spectrum was 0.068. Most of the error stemmed from visible wavelengths attributed to a "hook" in the observed data. Higher elevation albedo measurements were collected on 7 December 2022, at Mores Creek Summit (Boise Mountains) [see Figs. 6(b) and S.10]. The total RMSE for the modeled snow albedo across the entire spectrum was 0.050. The possible error could be due to a large solar zenith angle of 67.7° and nearby sloped terrain. On this same day at Mores Creek Summit, incoming solar irradiance was measured by pointing the ASD RCR straight up, plum from the Earth. The RMSE of optimal libRadtran modeled irradiance [i.e., optimal $E(\lambda)$ computed in (3)] was 2.08 μW cm^2 nm^{-1}sr^{-1} across all valid bands.

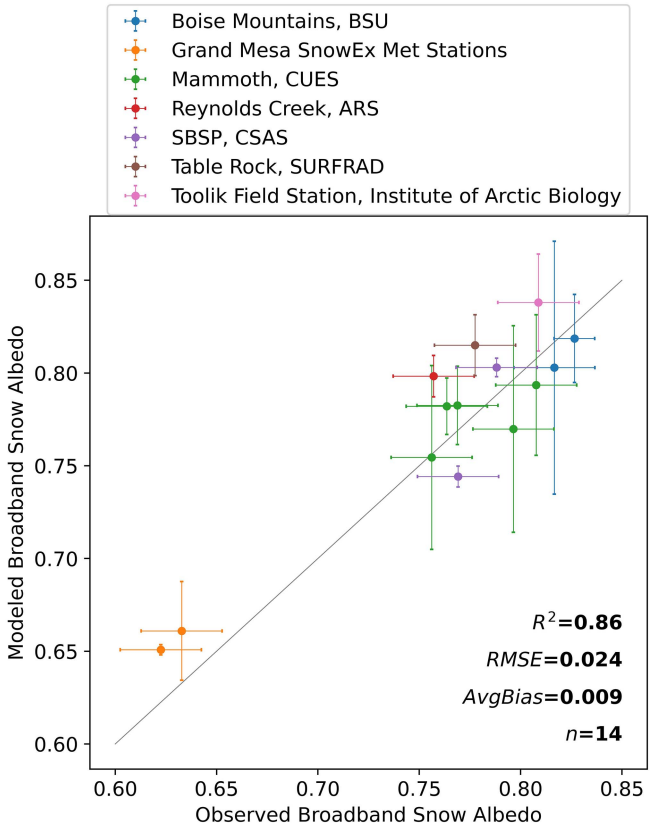

Fig. 5. Validation of snow broadband albedo for all sites. Vertical error bars represent the spatial variation of retrieved albedo around the pixel.

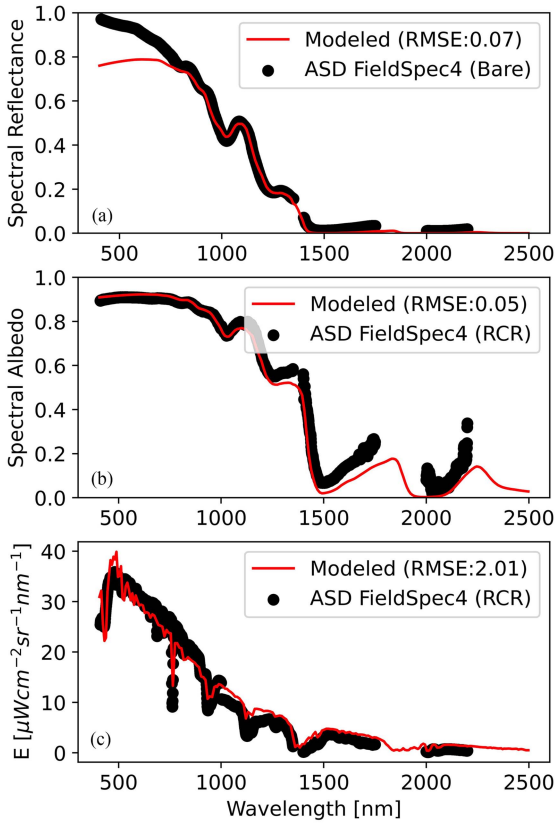

Fig. 6. (a) Modeled snow reflectance (red) versus ASD fieldspec4 (black) for 10 February 2022, (b) modeled spectral snow albedo versus ASD fieldspec4 for 8 December 2022, and (c) optimal spectral irradiance [E, via (3)] versus ASD fieldspec4 for 8 December 2022, all for Boise Mountains.

SSA was estimated as 43.1 m^2kg^{-1} for the interpolated pixel (1000 m spatial resolution), with an error ranging between 2.1 and 7.4 m^2kg^{-1} based on two colocated pits observed with IceCube during NASA SnowEx 2023 campaign around 15 March 2023 (see Fig. S.11). These observations were performed in dense boreal forest (canopy cover fraction $>$ 50%) and could possibly contribute to the error in retrieved SSA from our algorithm. More ground-based SSA observations are needed to draw more conclusive validation statistics on SSA performance.

For our fSCA validation, using a sample size of 2190 pixels on 8 December 2022, we found RMSE = 0.082, avg bias = −0.055, and F-stat = 1.0. In Fig. 7, we show the comparisons among the original PRISMA image, the airborne LiDAR fSCA, and the PRISMA-derived fSCA. The fSCA estimates have a negative bias, which is typical of most products for snow under forest, as it remains difficult to extract quality signal when canopy cover is high. Additionally, we are limited by the accuracy of maps of canopy cover fraction during the adjustment to fSCA. Higher quality canopy cover fraction maps could possibly improve the accuracy of fSCA.

V. Discussion

A. Comparison With Past Work and Potential Future Improvements

The results of our testing compare well with past research. Bair et al. [9] validated satellite retrieved albedo (using SPIRES with Moderate Resolution Imaging Spectroradiometer) against measurements at the Mammoth CUES site in California (USA) across three water years and found an average RMSE of 0.046. Our RMSE of 0.024 is comparable with Bair et al.'s article [9]. While our study uses fewer images, we include a range of snow conditions around the Northern Hemisphere (including Mammoth CUES). The mean bias reported by Bair et al. was 0.0067, which was similar to our findings of 0.009. This comparison highlights that both algorithms do not have a strong bias, positive or negative, despite using different grain shapes. For our study, the tower data were mostly flat and in the open. This is due in part because observing snow albedo on steep slopes remains a challenge [55]. More field measurements in steep topography and dense canopy conditions would improve our confidence in algorithm output over these regions and encourage algorithm development. For example, helpful work, such as the long-term monitoring at Col de Porte, France under dense canopy cover, may offer invaluable data for improvements in future snow property modeling [56], [57], [58].

In the current version of GOSHAWK, we programmatically select the two spectral endmembers based on the ESA WorldCover land cover map that is then related back to preselected EcoSpecLib_v1 spectral signatures collected in a lab. Future work could improve upon this by incorporating a more comprehensive spectral lookup library. For example, mixed boreal

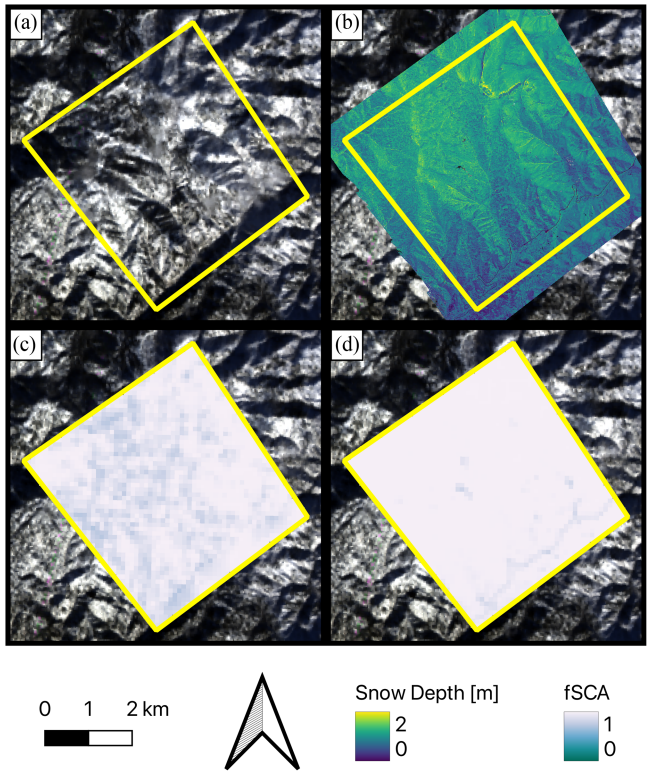

Fig. 7. (a) PRISMA L1 TOA radiance true colors 8 December 2022. (b) Airborne LiDAR-derived snow depth from 8 December 2022. (c) 100 m resolution fSCA from PRISMA. (d) 100 m resolution fSCA from LiDAR.

forests could be represented with spruce needles and birch branch spectra. Also, the snow classification map [17] could be used to select more appropriate spectral endmembers across landscapes. We also note that we did not implement BRDF effects into the vegetation endmembers; however, these effects are well studied [59]. Future improvement may also consider including these effects artificially on the pure endmembers based on information from the image and DEM.

Also, we used libRadtran to model the atmospheric state variables, but we note that this algorithm could theoretically use prebuilt MODTRAN lookup tables to increase operational usage and reliability. We decided to use libRadtran with the intention of building a public academic open-source tool, and the fact that libRadtran is well cited in the literature. Future works could adapt this framework to input MODTRAN or other radiative transfer modeling (e.g., ATCOR).

As for the issue of canopy cover, making progress on this area of snow cover mapping is vital to Earth system science, as forests make up approximately 40% of the snow-covered area in North America alone [60]. However, our linear spectral unmixing approximation does not make physical sense when transmission from the canopy is occurring. Nonlinear spectral unmixture approaches can be attempted in this case to improve model physics. Future work may also integrate complementary datasets with higher spatial resolution, with the cost of lower spectral resolution and potential temporal mismatch, such as Sentinel-2, to improve snow property retrieval under dense canopy.

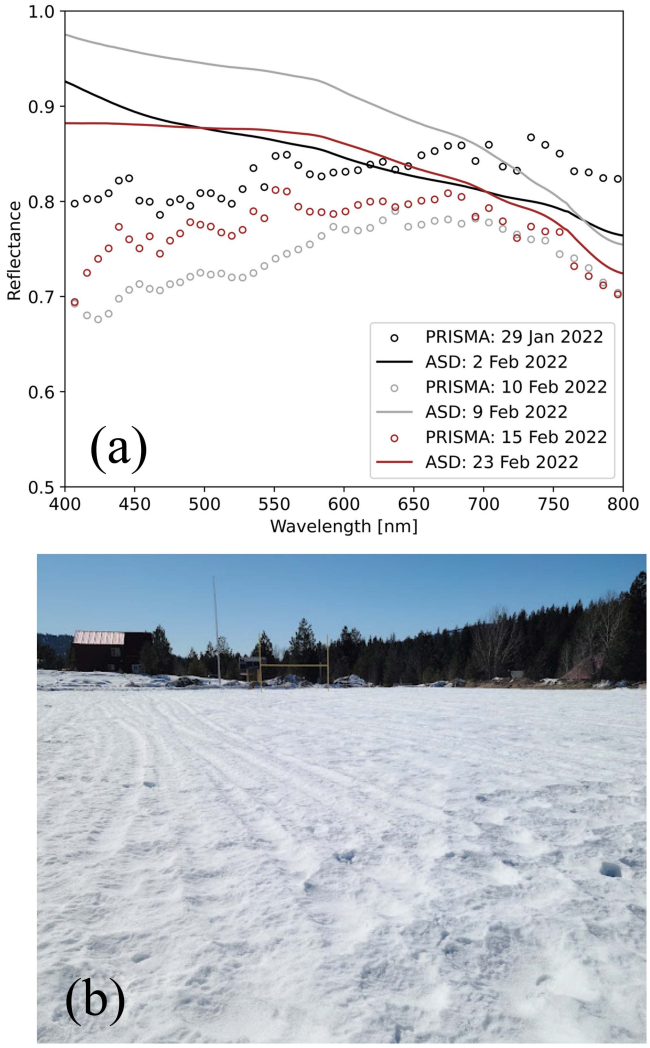

Fig. 8. ASD data collection at the Idaho City Boise Mountain site (b) with PRISMA and ASD surface reflectance overlaid for reference (a).

Given that the algorithm is an open-source project, the remote sensing community may use this as a starting point to make such changes. At the time of this publication, the original GOSHAWK algorithm is Version 1.0.0, and we anticipate future changes in follow-up releases. GOSHAWK is a globally appropriate algorithm that leverages high-performance computing. Our algorithm can currently process data from PRISMA and Earth Surface Mineral Dust Source Investigation (EMIT). GOSHAWK can be updated in the future to allow for data created by planned missions SBG and CHIME, provided a similar data structure. Consequently, this algorithm coupled with the increase in the number of available satellite imaging spectroscopy observations will enable more hydrologists, ecologists, and other scientists to have access to computing snow surface albedo and other optical snow properties.

B. Problematic Hook Impacts Applications That Rely on Shape and Magnitude of Visible Range

Work is needed to investigate the spatiotemporal relationships of the modeled snow albedo. For example, research that

examines snow albedo and snow cover with respect to forest disturbance and anthropogenic deposition in a changing climate [61], [62]. GOSHAWK open-source code can serve as a valuable resource for researchers and a starting point for these types of investigations. However, caution is advised on the reliability of inferring the concentration of light-absorbing particles from imaging spectroscopy measurements using current methods, such as GOSHAWK. For example, the ASD FieldSpec4 observed clean snow [see Fig. 6(b); Fig. S.6]; however, a "hooking" in the visible wavelengths can be seen from the PRISMA surface reflectance (see Fig. 8). Without correction of this hooking phenomena, modeled data could potentially overestimate light-absorbing particles' concentrations and underestimate albedo [63].

Recent studies have shown that DEM data derivatives, such as slope and aspect, have large errors [64]. These errors manifest in uncertainties of μ_s. A recent approach by Carmon et al. [40] has shown that the accurate estimates of μ_s can be retrieved as well using optimal estimation framework from the radiance data (i.e., treating μ_s as another unknown). It has been shown that successfully solving μ_s can greatly improve the hooking phenomena—by accounting for the correct proportion of direct to diffuse illumination [65]. However, while μ_s errors could lead to erroneous spectral shapes in steep terrain, it would not completely explain this specific case for our open field site [see Fig. 8(a)], where slope derived from Copernicus was on the order of 1° to 3°. While we did not take snow roughness measurements, Fig. 8(b) does show a fairly disturbed snow surface. This hooking phenomenon is not PRISMA specific and has been noted in other spaceborne and airborne sensors. This is currently an active area of research in the snow science community.

VI. Conclusion

In this work, we have established a new, globally applicable algorithm, GOSHAWK [66], to share with the greater snow science community. It is open source and is available on GitHub for use, modification, and collaboration. This method presents the first attempt at solving snow properties by k-means spectral clustering. The use of k-means spectral clustering has the benefit of reducing the dimensionality and computational cost of processing spaceborne imaging spectroscopy datasets while retaining high differentiation of spatial variability by grouping based on the cosine of the local solar illumination angle. This method was found to work well for a variety of snow classes across North America. Much work still remains in global snow algorithm development prelaunch of SBG and CHIME, especially in dense canopy and steep slopes. GOSHAWK methods and code may be a useful starting point for such future investigations.

Acknowledgment

The authors would like to thank the Italian Space Agency (ASI) for providing us access to PRISMA imagery and providing us the foundational data necessary for this research, A. Hedrick, D. Tappa, J. McNamara, and S. O'Neel for sharing invaluable ground data to support our validation efforts, and N. Bohn, N. Bair, J. Dozier, and A. Kokhanovsky for sharing code, data, and thoughts on modeling snow from space.

References

[1] P. Arias et al., "Climate change 2021: The physical science basis. contribution of working group i to the sixth assessment report of the intergovernmental panel on climate change; technical summary," 2021.
[2] S. Hassol, *Impacts of a Warming Arctic-Arctic Climate Impact Assessment*. Cambridge, U.K.: Cambridge Univ. Press, 2004.
[3] J. A. Screen and I. Simmonds, "The central role of diminishing sea ice in recent Arctic temperature amplification," *Nature*, vol. 464, no. 7293, pp. 1334–1337, 2010.
[4] G. Wendler and M. Shulski, "A century of climate change for Fairbanks, Alaska," *Arctic*, vol. 62, pp. 295–300, 2009.
[5] S. A. Rauscher, J. S. Pal, N. S. Diffenbaugh, and M. M. Benedetti, "Future changes in snowmelt-driven runoff timing over the western US," *Geophysical Res. Lett.*, vol. 35, no. 16, 2008, Art. no. L16703.
[6] X. Qu and A. Hall, "On the persistent spread in snow-albedo feedback," *Climate Dyn.*, vol. 42, pp. 69–81, 2014.
[7] Z. Li et al., "Accelerated multiphase water transformation in global mountain regions since 1990," *Innov. Geosci.*, vol. 1, no. 3, 2023, Art. no. 100033.
[8] C. Notarnicola, "Hotspots of snow cover changes in global mountain regions over 2000–2018," *Remote Sens. Environ.*, vol. 243, 2020, Art. no. 111781.
[9] E. H. Bair, T. Stillinger, and J. Dozier, "Snow property inversion from remote sensing (SPIReS): A generalized multispectral unmixing approach with examples from MODIS and Landsat 8 OLI," *IEEE Trans. Geosci. Remote Sens.*, vol. 59, no. 9, pp. 7270–7284, Sep. 2021.
[10] J. Dozier, S. R. Schneider, and D. F. M. G. Jr, "Effect of grain size and snowpack water equivalence on visible and near-infrared satellite observations of snow," *Water Resour. Res.*, vol. 17, no. 4, pp. 1213–1221, 1981.
[11] A. Kokhanovsky, B. Vandecrux, A. Wehrlé, O. Danne, C. Brockmann, and J. E. Box, "An improved retrieval of snow and ice properties using spaceborne OLCI/S-3 spectral reflectance measurements: Updated atmospheric correction and snow impurity load estimation," *Remote Sens.*, vol. 15, no. 1, 2022, Art. no. 77.
[12] S. G. Warren and W. J. Wiscombe, "A model for the spectral albedo of snow—II: Snow containing atmospheric aerosols," *J. Atmos. Sci.*, vol. 37, no. 12, pp. 2734–2745, 1980.
[13] G. Mie, "Beiträge zur optik trüber medien, speziell kolloidaler metallösungen," *Annalen Der Physik*, vol. 330, no. 3, pp. 377–445, 1908.
[14] Q. Libois et al., "Influence of grain shape on light penetration in snow," *Cryosphere*, vol. 7, no. 6, pp. 1803–1818, 2013.
[15] A. A. Kokhanovsky and E. P. Zege, "Scattering optics of snow," *Appl. Opt.*, vol. 43, no. 7, pp. 1589–1602, 2004.
[16] N. Bohn et al., "Optimal estimation of snow and ice surface parameters from imaging spectroscopy measurements," *Remote Sens. Environ.*, vol. 264, 2021, Art. no. 112613.
[17] M. Sturm and G. E. Liston, "Revisiting the global seasonal snow classification: An updated dataset for Earth system applications," *J. Hydrometeorol.*, vol. 22, no. 11, pp. 2917–2938, 2021.
[18] D. Zanaga et al., *ESA WorldCover 10 m 2020 v100*, 2021.
[19] C. DiMiceli, M. Carroll, R. Sohlberg, D. Kim, M. Kelly, and J. Townshend, "MOD44B MODIS/terra vegetation continuous fields yearly L3 global 250m SIN grid V006 [data set]," in *NASA EOSDIS Land Processes Distributed Active Archive Center*. Washington, DC, USA: NASA, 2015, doi: 10.5067/MODIS/MOD44B.006.
[20] J. Dozier and J. Frew, "Atmospheric corrections to satellite radiometric data over rugged terrain," *Remote Sens. Environ.*, vol. 11, pp. 191–205, 1981.
[21] T. Stillinger, D. A. Roberts, N. M. Collar, and J. Dozier, "Cloud masking for Landsat 8 and MODIS Terra over snow-covered terrain: Error analysis and spectral similarity between snow and cloud," *Water Resour. Res.*, vol. 55, no. 7, pp. 6169–6184, 2019.
[22] F. R. Valovcin, *Spectral Radiance of Snow and Clouds in the Near Infrared Spectral Region*, vol. 78. Bedford, MA, USA: Air Force Geophysics Laboratory, 1978.
[23] B. Mayer and A. Kylling, "The libRadtran software package for radiative transfer calculations-description and examples of use," *Atmos. Chem. Phys.*, vol. 5, no. 7, pp. 1855–1877, 2005.
[24] Y.-L. Dalcin, "Fang, mpi4py: Status update after 12 years of development," *Comput. Sci. Eng.*, vol. 23, no. 4, pp. 47–54, 2021, doi: 10.1109/MCSE.2021.3083216.

[25] R. P. Dalcin, M. Storti, and J. D'Elia, "MPI for Python: Performance improvements and MPI-2 extensions," *J. Parallel Distrib. Comput.*, vol. 68, no. 5, pp. 655–662, 2008, doi: 10.1016/j.jpdc.2007.09.005.
[26] J. B. Adams and A. R. Gillespie. *Remote Sensing of Landscapes With Spectral Images: A Physical Modeling Approach*. Cambridge, U.K.: Cambridge Univ. Press, 2018.
[27] E. H. Bair et al., "Divergence of apparent and intrinsic snow albedo over a season at a sub-alpine site with implications for remote sensing," *Cryosphere*, vol. 16, no. 5, pp. 1765–1778, 2022.
[28] S. K. Meerdink, S. J. Hook, D. A. Roberts, and E. A. Abbott, "The ECOSTRESS spectral library version 1.0," *Remote Sens. Environ.*, vol. 230, 2019, Art. no. 111196.
[29] D. A. Roberts, M. O. Smith, and J. B. Adams, "Green vegetation, nonphotosynthetic vegetation, and soils in AVIRIS data," *Remote Sens. Environ.*, vol. 44, no. 2/3, pp. 255–269, 1993.
[30] C. Quintano, A. Fernández-Manso, Y. E. Shimabukuro, and G. Pereira, "Spectral unmixing," *Int. J. Remote Sens.*, vol. 33, no. 17, pp. 5307–5340, 2012.
[31] G. Picard, Q. Libois, and L. Arnaud, "Refinement of the ice absorption spectrum in the visible using radiance profile measurements in Antarctic snow," *Cryosphere*, vol. 10, no. 6, pp. 2655–2672, 2016.
[32] S. G. Warren and R. E. Brandt, "Optical constants of ice from the ultraviolet to the microwave: A revised compilation," *J. Geophysical Res., Atmos.*, vol. 113, no. D14, pp. 1206–1225, 2008.
[33] C. Donahue, S. M. K. Skiles, and K. Hammonds, "Mapping liquid water content in snow at the millimeter scale: An intercomparison of mixed-phase optical property models using hyperspectral imaging and in situ measurements," *Cryosphere*, vol. 16, no. 1, pp. 43–59, 2022.
[34] D. J. Segelstein, "The complex refractive index of water," M.Sc. thesis, Dept. Phys., Univ. Missouri, Kansas City, MO, USA, 1981.
[35] D. Kraft, *A Software Package for Sequential Quadratic Programming—Deutsche Forschungs- und Versuchsanstalt fur Luft- und Raumfahrt*. DFVLR: Wiss. Berichtswesen d. DFVLR, 1988.
[36] A. A. Kokhanovsky, "The broadband albedo of snow," *Front. Environ. Sci.*, vol. 9, 2021, Art. no. 757575.
[37] T. Stillinger, K. Rittger, M. S. Raleigh, A. Michell, R. E. Davis, and E. H. Bair, "Landsat, MODIS, and VIIRS snow cover mapping algorithm performance as validated by airborne lidar datasets," *Cryosphere*, vol. 17, no. 2, pp. 567–590, 2023.
[38] S. Cogliati et al., "The PRISMA imaging spectroscopy mission: Overview and first performance analysis," *Remote Sens. Environ.*, vol. 262, 2021, Art. no. 112499.
[39] A. Chlus, M. Gierach, and P. A. Townsend, *EnSpec/sister: 1.0.0 (1.0.0)*. Genève, Switzerland: Zenodo, 2022, doi: 10.5281/zenodo.5997779.
[40] N. Carmon et al., "Shape from spectra," *Remote Sens. Environ.*, vol. 288, 2023, Art. no. 113497.
[41] Center for Snow and Avalanche Studies, *Archival Data From Senator Beck Basin Study Area*, 2023. [Online]. Available: https://snowstudies.org/archived-data/
[42] Environmental Data Center Team, *Meteorological Monitoring Program at Toolik, Alaska. Toolik Field Station*, *Institute of Arctic Biology*, *University of Alaska Fairbanks*, Fairbanks, AK, USA, 2023. [Online]. Available: https://toolik.alaska.edu/edc/monitoring/abiotic/met-data-query.php
[43] *Snow Research at UC Santa Barbara and The Cold Regions Research and Engineering Laboratory (CRREL) and University of California Santa Barbara (UCSB) Energy Site*, 2023, doi: 10.21424/R4159Q.
[44] J. A. Augustine, J. J. DeLuisi, and C. N. Long, "SURFRAD—A national surface radiation budget network for atmospheric research," *Bull. Amer. Meteorol. Soc.*, vol. 81, no. 10, pp. 2341–2358, 2000.
[45] P. Houser et al., "SnowEx meteorological station measurements from Grand Mesa, CO, version 1," in *NASA National Snow and Ice Data Center Distributed Active Archive Center*. Washington, DC, USA: NASA, 2022.
[46] B. A. Wilder, J. Enterkine, H.-P. Marshall, T. van der Weide, and N. F. Glenn, "Dataset for ASD FieldSpec4 snow and conifer measurements in Idaho and Colorado (2022-2023)," 2023. [Online]. Available: https://scholarworks.boisestate.edu/bcal_data/7/
[47] 2024. [Online]. Available: https://www.apogeeinstruments.com/content/SN-500-spec-sheet.pdf
[48] C. M. Carmagnola et al., "Snow spectral albedo at Summit, Greenland: Measurements and numerical simulations based on physical and chemical properties of the snowpack," *Cryosphere*, vol. 7, no. 4, pp. 1139–1160, 2013.
[49] T. C. Grenfell, S. G. Warren, and P. C. Mullen, "Reflection of solar radiation by the Antarctic snow surface at ultraviolet, visible, and near-infrared wavelengths," *J. Geophysical Res., Atmos.*, vol. 99, no. D9, pp. 18669–18684, 1994.
[50] D. Helder et al., "Recent surface reflectance measurement campaigns with emphasis on best practices, SI traceability and uncertainty estimation," *Metrologia*, vol. 49, no. 2, 2012, Art. no. S21.
[51] J. Meloche et al., *SnowEx23 Laser Snow Microstructure Specific Surface Area Data, Version 1 [Data Set]*. Boulder, CO USA: NASA, 2023, doi: 10.5067/BSEP59ADC6XN.
[52] S. O'Neel et al., "Helicopter-borne lidar to resolve snowpack variability in southwest Idaho," *AGU Fall Meeting Abstr.*, vol. 2022, pp. C35E–0922, 2022.
[53] R. A. Beyer, O. Alexandrov, and S. McMichael, "The Ames stereo pipeline: NASA's open source software for deriving and processing terrain data," *Earth Space Sci.*, vol. 5, no. 9, pp. 537–548, 2018.
[54] Z. Hoppinen, B. Wilder, S. O'Neel, and N. Adebisi, *SnowEx/Ice-Road-Copters: V1.0.0 (v1.0.0)*. Genève, Switzerland: Zenodo, 2023, doi: 10.5281/zenodo.8184592.
[55] G. Picard et al., "Spectral albedo measurements over snow-covered slopes: Theory and slope effect corrections," *Cryosphere*, vol. 14, no. 5, pp. 1497–1517, 2020.
[56] J. E. Sicart et al., "Snow accumulation and ablation measurements in a mid-latitude mountain coniferous forest (Col de Porte, France, 1325 m alt.): The snow under forest field campaigns dataset," *Earth Syst. Sci. Data Discuss.*, vol. 2023, pp. 1–22, 2023.
[57] S. Morin et al., "An 18-yr long (1993–2011) snow and meteorological dataset from a mid-altitude mountain site (Col de Porte, France, 1325 m alt.) for driving and evaluating snowpack models," *Earth Syst. Sci. Data*, vol. 4, no. 1, pp. 13–21, 2012.
[58] Y. Lejeune et al., "57 years (1960–2017) of snow and meteorological observations from a mid-altitude mountain site (Col de Porte, France, 1325 m of altitude)," *Earth Syst. Sci. Data*, vol. 11, no. 1, pp. 71–88, 2019.
[59] W. Jia, Y. Pang, R. Tortini, D. Schläpfer, Z. Li, and J.-L. Roujean, "A kernel-driven BRDF approach to correct airborne hyperspectral imagery over forested areas with rugged topography," *Remote Sens.*, vol. 12, no. 3, 2020, Art. no. 432.
[60] A. G. Klein, D. K. Hall, and G. A. Riggs, "Improving snow cover mapping in forests through the use of a canopy reflectance model," *Hydrol. Processes*, vol. 12, no. 10/11, pp. 1723–1744, 1998.
[61] Z. Wang et al., "Early spring post-fire snow albedo dynamics in high latitude boreal forests using Landsat-8 OLI data," *Remote Sens. Environ.*, vol. 185, pp. 71–83, 2016.
[62] P. D. Micheletty, A. M. Kinoshita, and T. S. Hogue, "Application of MODIS snow cover products: Wildfire impacts on snow and melt in the Sierra Nevada," *Hydrol. Earth Syst. Sci.*, vol. 18, no. 11, pp. 4601–4615, 2014.
[63] C. P. Donahue et al., "Bridging the gap between airborne and spaceborne imaging spectroscopy for mountain glacier surface property retrievals," *Remote Sens. Environ.*, vol. 299, 2023, Art. no. 113849.
[64] J. Dozier et al., "Error and uncertainty degrade topographic corrections of remotely sensed data," *J. Geophysical Res., Biogeosci.*, vol. 127, no. 11, 2022, Art. no. e2022JG007147.
[65] N. Bohn et al., "Estimating dust on snow-application of a coupled atmosphere-surface model to spaceborne emit imaging spectrometer data," in *Proc. IEEE Int. Geosci. Remote Sens. Symp.*, 2023, pp. 685–688.
[66] B. Wilder, *Cryogars/GOSHAWK: Initial Release (v1.0.0)*. Genève, Switzerland: Zenodo, 2024, doi: 10.5281/zenodo.10652710.

Brenton A. Wilder received the B.S. degree (*Kellogg Honors College Graduate*) in civil engineering from California State Polytechnic University, Pomona, CA, USA, in 2018, and the M.S. degree in civil engineering (specialization in water resources engineering) from San Diego State University, San Diego, CA, USA, in 2021. He is currently working toward the Ph.D. degree in geosciences with the Department of Geosciences, Boise State University, Boise, ID, USA.

Christine M. Lee received the B.S. degree in chemical engineering with a minor in English and the M.S. and Ph.D. degrees in civil and environmental engineering from the University of California, Los Angeles (UCLA), Los Angeles, CA, USA, in 2005, 2006, and 2010, respectively.

With NASA JPL, she is an ECOSTRESS Applications Lead, SBG Co-Lead Applications, Visiting Associate Scientist with UCLA, and the Technical Group Supervisor of the Water and Ecosystems Group.

Adam Chlus received the B.S. degree in environmental science and the M.S. degree in natural resources from the University of Connecticut, Storrs, CT, USA, in 2011 and 2015, respectively, and the Ph.D. degree in forestry from the University of Wisconsin, Madison, WI, USA, in 2020.

He was a Postdoctoral Scholar and is currently a Research Technologist with NASA JPL, where he is developing and implementing algorithm workflows for airborne and spaceborne imaging spectroscopy data.

Hans-Peter Marshall received the B.S. degree in physics with a minor in geophysics from the University of Washington, Washington, DC, USA, in 1999, and the Ph.D. degree in civil engineering with an emphasis in geotechnical engineering from the University of Colorado Boulder, Boulder, CO, USA, in 2005.

He is a Professor with the Department of Geosciences and the Co-Director of the Cryosphere Geophysics and Remote Sensing Group with Boise State University, Boise, ID, USA. He is a snow Scientist and Glaciologist who uses geophysics and engineering tools to study the cryosphere. He was a visiting Ph.D. student for one winter with the Swiss Federal Institute for Snow and Avalanche Research in 2004. His current research with Boise State University is focused on spatial variability in snow and its effect on remote sensing, snow hydrology, and snow avalanches.

Dr. Marshall was a recipient of the 2010 AGU Cryosphere Focus Group's Young Investigator Award.

Jodi Brandt received the B.A. degree in geology/geophysics from Yale University, New Haven, CT, USA, in 1996, the M.S. degree in environmental sciences from the University of Maryland, MD, USA, in 2004, and the Ph.D. degree in forest and wildlife ecology from the University of Wisconsin, Madison, WI, USA, in 2012.

He is a land use Scientist with a primary focus on drought adaptation, farmland protection, and biodiversity conservation. She leads multidisciplinary teams funded by NASA, USDA, NSF, and state agencies. Her research has been published in *Science*, *PNAS*, *Remote Sensing of Environment*, *Conservation Biology*, *Land Use Policy,* and various other high-impact journals. She is an Associate Professor of human-environment systems with Boise State University, Boise, ID, USA.

Alicia M. Kinoshita received the B.S. degree in civil engineering with a minor in classical civilizations and the M.S. and Ph.D. degrees in civil engineering from the University of California, Los Angeles, Los Angeles, CA, USA, in 2007, 2009, and 2012, respectively.

She was a Postdoctoral Scholar in civil and environmental engineering with the Colorado School of Mines, Golden, CO, USA, from 2012 to 2014. She is an Associate Professor with the Department of Civil, Construction, and Environmental Engineering and the Director of Undergraduate Research and Creative Activities, San Diego State University, San Diego, CA, USA. Her research group focuses on understanding and modeling water resources and hydrologic processes after disturbances, such as wildfires in watersheds across the Western United States. Her work is supported by agencies, such as the National Science Foundation, the National Aeronautics and Space Administration, and the San Diego River Conservancy.

Dr. Kinoshita was a recipient of an NSF CAREER Award to study the urban Mediterranean systems after fire.

Josh Enterkine received the B.A. degree (*cum laude*) in environmental studies with a minor in anthropology and the M.S. degree in geosciences from Boise State University, Boise, ID, USA, in 2011 and 2019, respectively.

He serves as a Remote Sensing Research Associate with the Department of Geosciences, Boise State University, the Lab Manager for Boise Center Aerospace Laboratory, and the Chair of the Idaho Elevation Technical Working Group.

Thomas Van Der Weide received the B.S. and M.S. degrees in geophysics from Boise State University, Boise, ID, USA, in 2016 and 2019, respectively.

He works as a Research Associate with the Department of Geosciences, Boise State University. His research focus so far has concentrated on accurately mapping the snowpack using a range of sensors on unmanned aerial vehicles.

Nancy F. Glenn received the B.S. degree in geological engineering from the University of Nevada, Reno, NV, USA, in 1994, the M.S. degree in geotechnical/civil engineering from the University of California, Berkeley, CA, USA, in 1996, and the Ph.D. degree in geoengineering from the University of Nevada, Reno, NV, USA, in 2000.

She is a Professor of geosciences with Boise State University, Boise, ID, USA, and leads interdisciplinary remote sensing research in her lab, Boise Center Aerospace Laboratory. She is a Licensed Professional Engineer in the state of Idaho, USA (#14023). He also serves as the Vice President of Research and Economic Development with Boise State University and was the Founding Co-Director of Boise State's Human-Environment Systems in the new College of Innovation and Design. She also serves on the NASA Headquarters Earth Science Advisory Committee.